ROYAL SOCIETY
OF CHEMISTRY

COMMUNICATION

Check for updates

Inverted planar solar cells based on perovskite/graphene oxide hybrid composites†

Chih-Chun Chung, Sudhakar Narra, Efat Jokar, Hui-Ping Wu and Eric Wei-Guang Diau*

Mixing graphene oxide (GO) with $CH_3NH_3PbI_3$ (PSK) in varied proportions (0.025, 0.05 and 0.075 mg mL^{-1}) and using GO nanosheets as a p-type electrode for devices with a layer-by-layer thin-film configuration ITO/GO/PSK:GO/PCBM/Ag produced hybrid composite perovskite solar cells. The efficiency of power conversion (PCE) of the device prepared with GO in PSK solution (0.05 mg mL^{-1}) attained 15.2%, which is greater than that of a conventional planar heterojunction device (PCE 12.3%) fabricated using pristine PSK. In the homogeneous PSK:GO active layers, PSK acted as a hole donor and GO as a hole acceptor. The optimum GO concentration (0.05 mg mL^{-1}) increased the charge mobility (investigated using Hall effect measurements), enhanced the charge separation (investigated using photoluminescence decays) and retarded the charge recombination (investigated using electrochemical impedance spectra), consistent with the trend of corresponding device performances. Our results thus indicate that the hybrid PSK:GO layer increased the interfacial contact between the donor and acceptor of holes to balance the charge mobility and improved the photovoltaic performance with excellent reproducibility and stability.

Introduction

Organic–inorganic methylammonium lead halide perovskites (PSKs) exhibit an excellent light-harvesting ability and attract much attention as high-performance next-generation solar cells.[1–14] To further enhance the efficiency of photo-conversion, one should, however, consider the intrinsic properties of perovskite materials, such as the defect sites of crystals, their ferroelectric properties, the unbalanced mobility of charge carriers and the electro-migration of ions.[15–18] In addition to intrinsic perovskite properties, the device structure affects the

device performance. High performance devices have been reported with both regular (n–i–p) and inverted (p–i–n) film configurations, as well as with various charge-transport materials.[10–13] Due to the ambipolar properties of these materials, perovskite crystals can transport both charge carriers (electrons and holes) simultaneously[19] and so they can be utilized for fabricating planar heterojunction (PHJ) solar cells. Inverted PHJ perovskite solar cells were investigated *via* simple solution-based fabrication of a device at low temperature, which is feasible for flexible photovoltaic applications.[20]

Balancing the electron and hole mobilities is an effective approach to improve the efficiency of PHJ perovskite solar cells, for which the diffusion length of the holes in such a device is greater than that of the electrons.[21,22] As a result, a traditional donor–acceptor bulk heterojunction configuration has been considered in organic solar cells that can enhance the interfacial contact to improve the charge separation significantly.[23–25] Among the few reports of the hybrid composite concept for perovskite solar cells,[26–29] heterojunction contact engineering was introduced by blending an electron acceptor such as PCBM inside PSK to improve both the quality of the perovskite films and the efficiency of electron extraction.

The charge-transport layer is another parameter that plays a significant role in improving the overall performance of PHJ perovskite solar cells. In an inverted configuration, the hole-extraction layer (HEL) serves as the first component interacting with light substantially and so its optical properties are important. Conducting polymer PEDOT:PSS and its derivatives have traditionally served as the hole-extraction layer to increase the hole-collection properties of OPV[30,31] or inverted PHJ perovskite solar cells,[32,33] but the detrimental effects of its acidity, hygroscopic properties and inhomogeneous electricity make the long-term stability of devices using PEDOT:PSS as the p-contact electrode a critical issue.[34,35] Graphene oxide (GO) and its derivative materials have been widely applied in photovoltaic devices because of their excellent intrinsic optical and electronic properties.[36] The optical and electrical properties of GO can be controlled and modified by its surface chemistry. The

Department of Applied Chemistry, Institute of Molecular Science, National Chiao Tung University, No. 1001, Ta-Hsueh Rd, Hsinchu 30010, Taiwan. E-mail: diau@mail.nctu.edu.tw

This journal is © The Royal Society of Chemistry 2017

J. Mater. Chem. A, 2017, 5, 13957–13965 | 13957

excellent dispersion of GO in many common solvents, the cheap and solution-based processes and the excellent stability are other advantages that attract significant interest in the field of solar cells.[37–40]

Herein we combined both concepts, (1) using GO to replace PEDOT:PSS as a promising transparent p-contact electrode, and (2) blending GO efficiently into PSK to form a PSK:GO hybrid composite layer, to fabricate high-performance inverted perovskite solar cells with device configuration ITO/GO/PSK:GO/PCBM/Ag. Graphene oxide acts not only as an efficient hole-extraction layer but also as a hole acceptor in the hybrid PSK:GO composites. On varying the amount of GO inside the perovskite film (0.025, 0.05 and 0.075 mg mL^{-1}), we found that the PSK:GO solar cell (0.05 mg mL^{-1}) exhibited the best efficiency of 15.2%, which is superior to that of a conventional PSK solar cell (PCE 12.3%). Measurements of the Hall effect, photoluminescence (PL) spectra, time-correlated single-photon counting (TCSPC) and electrochemical impedance spectral (EIS) results showed that GO is an efficient hole acceptor inside the perovskite layer to balance electron and hole mobility, thereby enhancing the charge separation and decreasing the charge recombination, consistent with the trend observed for the corresponding photovoltaic performance. The present work provides the first demonstration of inverted perovskite solar cells using GO as both the hole-extraction layer and hole acceptor in the PSK:GO active layer.

Results and discussion

Graphene oxide was prepared according to a modified Hummers' method;[41] the details are given in the Experimental section. The formation of GO was confirmed with Raman and FTIR spectra (Fig. S1a and b, ESI,† respectively). GO was dispersed in DMF to prepare a stock solution of 0.5 mg mL^{-1} concentration. Varied portions of the PSK:GO solutions were prepared by mixing the GO stock solutions with the PSK solutions in DMF with the concentration of PSK maintained at 45 mass% in 1 mL. With volume ratios of 5, 10 and 15% of the GO stock solutions prepared in the PSK:GO precursor solutions, the mass concentrations of GO in 45 mass% PSK of total volume 1 mL were 0.025, 0.05 and 0.075 mg mL^{-1}, respectively. Fig. S2a and b, ESI,† show the absorption spectra of the PSK:GO precursor solutions and the corresponding thin-film samples after spin-coating and solvent-annealing procedures.[6,42] The inverted perovskite/GO hybrid composite solar cells were fabricated according to device configuration ITO/GO/PSK:GO/PCBM/Ag as shown in Fig. 1a; the corresponding potential energy levels of each layer are shown in Fig. 1b. A thin layer of GO (as shown in the SEM image in Fig. S3, ESI†) served as an efficient HEL; this conventional planar perovskite solar cell was reported to attain a PCE of 12.4%,[39] superior to that of one with PEDOT:PSS as the HEL reported in the same article. In the present work, we used a pristine perovskite device as a reference to compare the PV performance with those of other perovskite/GO hybrid composite devices.

Fig. 2a–d show the SEM images of perovskite layers produced with precursor solutions containing GO at concentrations of 0,
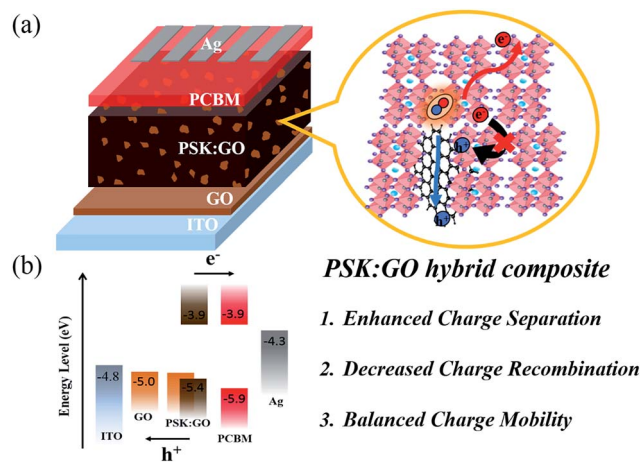

Fig. 1 (a) Architecture of inverted perovskite solar cells with the PSK:GO hybrid composite; (b) energy-level diagram of the corresponding materials.

0.025, 0.05 and 0.075 mg mL^{-1}, respectively; the corresponding top-view images appear in the insets of each figure. The SEM images show that uniform, smooth, and pin-hole-free PSK films with well-crystallized and well-packed grains are formed. Even with the same procedure to fabricate the perovskite films, the film thickness systematically increased from 310 nm (without GO) to 380 nm (with GO, 0.075 mg mL^{-1}), consistent with the corresponding absorption spectra shown in Fig. S2b, ESI.† The SEM top-view images show that all pristine and GO-hybrid PSKs had similar crystal morphologies, confirmed by the AFM topographical images in Fig. S4, ESI.† The crystallinity of these PSK samples was confirmed by XRD data (Fig. S5, ESI†), showing that these PSK nanocrystals all have high crystallinity in a single phase. To determine whether GO nanosheets are evenly distributed inside the PSK:GO composites, we employed the elemental mapping of energy-dispersive X-ray spectra (EDX) to investigate the depth profile of GO. Here cysteamine (NH_2-CH_2CH_2SH)-modified GO nanosheets were blended with PSK so as to allow us to use S as a tracing element. The EDX mapping results shown in Fig. S6, ESI,† indicate that the PSK:GO layer has a homogeneous distribution of GO inside the entire PSK layer.

Fig. 3a and b present the $J-V$ characteristics and IPCE action spectra of the inverted perovskite solar cells, respectively, with the device configuration shown in Fig. 1a for the PSK active layers fabricated with graphene oxide at concentrations of 0, 0.025, 0.05 and 0.075 mg mL^{-1}; the corresponding photovoltaic parameters are summarized in Table 1. The photovoltaic performances of the perovskite/GO hybrid composite devices improved systematically relative to a pristine perovskite device (without GO blending) from small to moderate GO concentrations, but degraded at a large GO concentration. The best PSK:GO hybrid composite device was the one with a GO concentration of 0.05 mg mL^{-1}, showing the PCE of 15.2% with J_{SC} of 20.71 mA cm^{-2}, V_{OC} of 959 mV and FF of 0.763; the efficiency is ~25% greater than that of the pristine perovskite device (PCE 12.3%), which is comparable with those of other
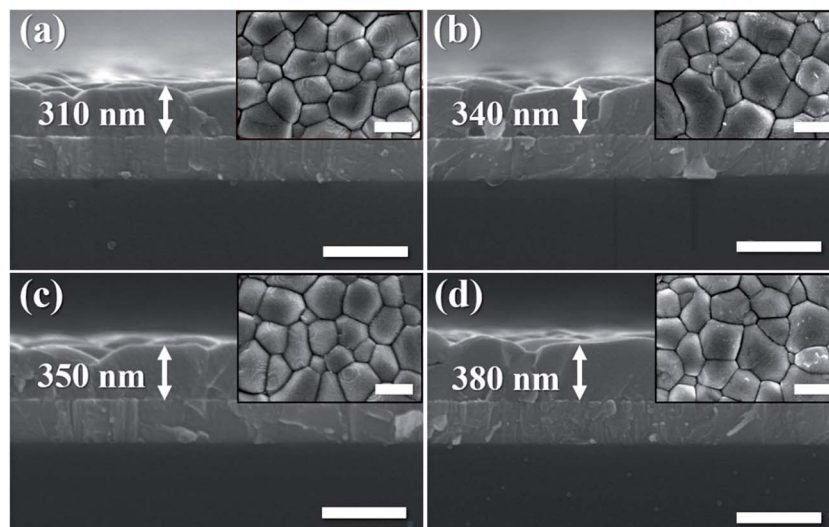
Fig. 2 Side-view SEM images of (a) pristine PSK layer, (b) PSK:GO (0.025 mg mL^{-1}) layer, (c) PSK:GO (0.05 mg mL^{-1}) layer and (d) PSK:GO (0.075 mg mL^{-1}) layer; the insets show the top-view SEM images of the corresponding perovskite films. All scale bars represent 500 nm.
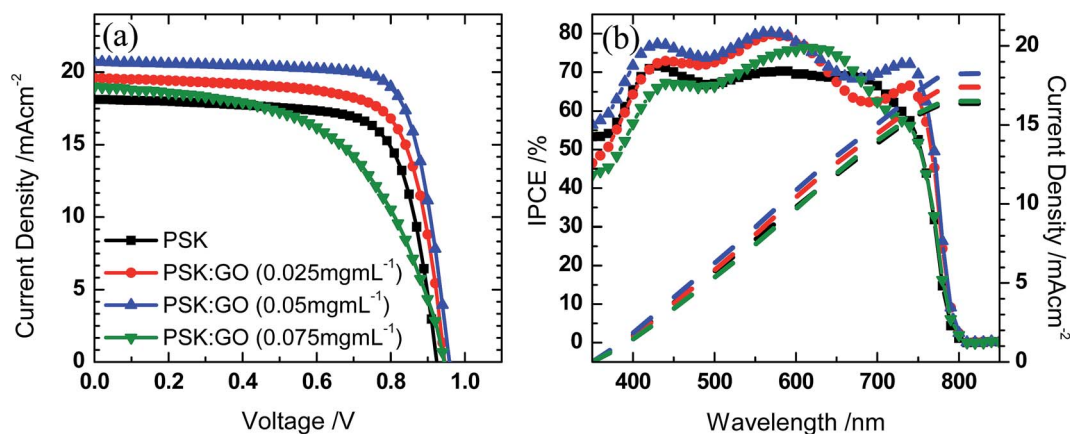

Fig. 3 (a) J–V characteristics of PSK and PSK:GO perovskite solar cells under AM 1.5G simulated illumination. (b) IPCE spectra of PSK and PSK:GO perovskite solar cells.

GO-based perovskite solar cells.[38,39] The enhanced photovoltaic performances of the PSK:GO hybrid composite devices are attributed to the increased interfaces inside the hybrid PSK:GO active layer that enable efficient charge separation, but further increase of GO concentration to 0.075 mg mL^{-1} led to a poor dispersion of GO in the PSK:GO solutions causing the formation of a poor film morphology on a large scale (Fig. S7, ESI†) and significant degradation of the FF of the solar cells. We examined the effect of hysteresis which is a typical problem in perovskite solar cells.[15–18] Fig. S8, ESI,† shows the J–V characteristics of both pristine PSK and PSK:GO hybrid composite (0.05 mg mL^{-1}) devices in varied scan directions as indicated; Fig. S9, ESI,† shows the J–V curves of the PSK:GO hybrid composite (0.05 mg mL^{-1}) device with delay intervals of 10–300 ms. Our results show almost no hysteresis effect for all the JV curves under investigations, which indicates that the interfacial contact between constituent layers in both devices was optimized.

Fig. 3b shows the IPCE spectra with a broad spectral response in the range of 350–800 nm, which agrees with the absorption spectra of perovskite thin films (Fig. S2b, ESI†); the integrated current densities correlate closely with the photo-currents in the J–V characteristics. The PSK:GO hybrid composite device (0.05 mg mL^{-1} GO) exhibits a strong response over the entire visible spectral region. Relative to the pristine PSK device, the enhanced IPCE of the PSK:GO hybrid composite perovskite solar cells originates from the contribution of graphene oxide inside the hybrid PSK:GO layer. To confirm that the enhancements in J_{SC} and PCE are due to the PSK:GO hybrid composite structure rather than an increased thickness of the perovskite film observed in Fig. 2, we performed control experiments on increasing the film thickness of the pristine PSK under the same experimental conditions but with greater precursor concentrations (e.g. 47 and 50 mass%). The side-view SEM images and the photovoltaic results appear in Fig. S10 and S11, ESI,† respectively; the photovoltaic results are summarized

This journal is © The Royal Society of Chemistry 2017

J. Mater. Chem. A, 2017, **5**, 13957–13965 | **13959**

Table 1 Photovoltaic parameters, resistances and mobility of the pristine PSK and the PSK:GO hybrid composite inverted perovskite solar cells based on composite layers with graphene oxide at varied concentrations

Devices	J_{SC}/mA cm^{-2}	V_{OC}/mV	FF	PCE/%	$R_{SH}{}^{a}$/Ω cm^2	$R_1{}^{b}$/Ω cm^2	Mobility^{c}/cm^2 V^{-1} s^{-1}
PSK	18.11	927	0.731	12.3	8865	75.5	28.6
PSK:GO (0.025)^{d}	19.59	945	0.730	13.5	9414	79.4	32.5
PSK:GO (0.05)^{d}	20.71	959	0.763	15.2	99 978	313.4	35.3
PSK:GO (0.075)^{d}	19.02	930	0.651	11.5	23 144	176.5	34.7

[a] Shunt resistance obtained from the J–V curves is shown in Fig. 3a. [b] Charge recombination resistance obtained from the EIS spectra is shown in Fig. 5. [c] Electron mobility is obtained from Hall effect measurements. [d] Concentration (mg mL^{-1}) of GO in the PSK:GO hybrid composite layers.

in Table S1, ESI.† The results of the control experiments show that J_{SC} values increased with increasing thickness of the PSK film, but the overall performances of the pristine PSK devices of greater film thickness suffered from degraded V_{OC} and FF, likely because of limited carrier transport in thicker PSK layers. Comparing between pristine PSK and PSK:GO hybrid composite devices with a PSK layer of the same thickness (340 nm), the device with GO at 0.05 mg mL^{-1} performed much better than the pristine PSK device, confirming the important role of GO in improving the performance of a composite architecture. Moreover, we have carried out experiments for pristine PSK and the PSK:GO hybrid composite (0.05 mg mL^{-1}) deposited on the PEDOT:PSS electrode and then made the corresponding devices for comparison. For each type of solar cell, twenty devices were fabricated under the same experimental conditions and their device performances are shown in Fig. S12;† the corresponding photovoltaic parameters of these two types of devices are listed in Tables S2–S4, ESI.† For the PEDOT:PSS devices, we also observed an enhancement in V_{OC} and FF for the PSK:GO hybrid composite devices compared to the pristine PSK devices, similar to the results of GO-based solar cells. From these consistent results, we may conclude that the enhanced photovoltaic performance of the devices made of the PSK:GO hybrid composite is a general phenomenon for inverted perovskite solar cells; the reasons are given below.

The significantly improved photovoltaic performance of the PSK:GO hybrid composite device indicates that the charge-carrier mobility inside the PSK:GO might be more balanced for the PSK:GO hybrid composites than for the pristine PSK perovskite solar cells.[43] The intrinsic carrier mobility of the PSK:GO hybrid composites was evaluated from measurements of the Hall effect; the results are summarized in Table 1. The values of electron mobility exhibit a trend with increasing GO concentration until 0.05 mg mL^{-1}, consistent with the trend of the device performances. The Hall coefficients (from -0.0181 to -0.0214) were negative, confirming the enhanced n-type properties of our pristine PSK and PSK:GO hybrid composite devices. The carrier concentrations were determined based on the formula $n = \dfrac{-B_z I}{d V_H Q}$, in which B_z denotes the magnetic field, I the DC electric current, d the sample thickness, V_H the Hall voltage, and Q the electronic charge. As shown in Table S5, ESI,† the carrier concentrations (n) are of order 10^{20} cm^{-3}, similar to those in solution-processed films.[44] The value of n for the PHJ perovskite film was greater than that for a single crystal of

perovskite, which implies more trapping sites of nearly intrinsic semiconducting behavior in the PSK nanocrystals.[45] The introduction of GO into the perovskite layer slightly decreases the amount of electron density that is explicable according to the effect of passivation of defect sites of the perovskite in the presence of GO. The values of electron mobility in the PSK:GO hybrid composite films listed in Table 1 agree with the reported values[46–48] for highly efficient photovoltaic devices made with crystalline films of great mobility.[6,7] Because blending GO into the PSK layer increases the charge mobility and decreases the concentration of charge carriers to decrease the trap states for retarded charge recombination, the presence of GO in PSK with a hybrid heterojunction structure induces efficient charge separation and creates a balance between the two charge carriers.

The steady-state photoluminescence (PL) spectra and the corresponding PL decays of PSK and the hybrid PSK:GO thin-film samples are shown in Fig. 4a and b, respectively. All PL spectra exhibit a sharp excitonic emission band with a maximum at 770 nm. The PL intensities show the order PSK > PSK:GO (0.075 mg mL^{-1}) > PSK:GO (0.025 mg mL^{-1}) > PSK:GO (0.05 mg mL^{-1}), indicating that effective PL quenching occurred inside the hybrid PSK:GO layer with small and moderate GO concentrations. In contrast, the intensity of PL is greater at a GO concentration of 0.075 mg mL^{-1} than for the other PSK:GO devices, indicating that PL quenching due to charge separation becomes less efficient when the GO concentration increases. The PL intensities serve as indirect markers of the lifetimes of the excitons produced in these samples, but direct evidence is derived from measurement of the PL decay kinetics of these samples using the TCSPC technique. As shown in Fig. 4b, the normalized PL transients ($\lambda_{ex} = 635$ nm and $\lambda_{PL} = 770$ nm) exhibit a decay feature with a trend similar to the trend of PL quenching as shown in Fig. 4a. These PL transients were fitted using a multi-exponential decay function; the corresponding time coefficients (relative amplitudes in parentheses) are summarized in Table S6, ESI.†

For pristine PSK, two decay components sufficed for the fit: the first decay component ($\tau_1 = 24$ ns) corresponds to non-radiative surface-state relaxation of PSK, and the second decay component ($\tau_2 = 429$ ns) is attributed to recombination in the bulk.[49,50] In contrast, all PL transients of the PSK:GO samples require three decay components for a satisfactory fit. Relative to the pristine PSK sample, the values of the first decay coefficient (τ_1) are one tenth of those of the PSK:GO samples with the order

13960 | *J. Mater. Chem. A*, 2017, **5**, 13957–13965

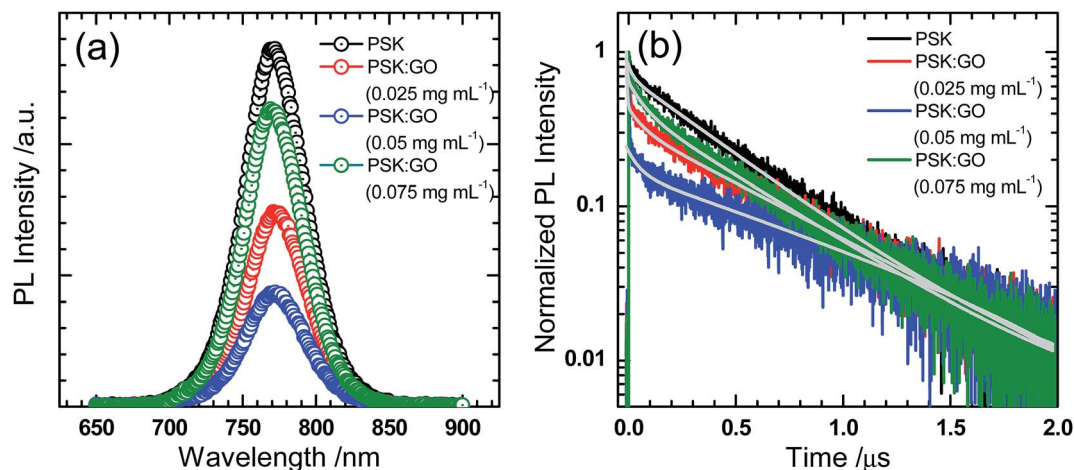This journal is © The Royal Society of Chemistry 2017

Fig. 4 (a) Photoluminescence spectra and (b) transient photoluminescence of either pristine PSK or the PSK:GO hybrid composite layer with progressively varied GO ratio (red, blue, and green) compared with those of the control sample (black).

τ_1 (0.05 mg mL^{-1}) < τ_1 (0.025 mg mL^{-1}) < τ_1 (0.075 mg mL^{-1}), consistent with the trend observed for the PL quenching. The rapid non-radiative relaxation of the hybrid PSK:GO samples indicates that hole injection from PSK into GO in the PSK:GO hybrid composite structure is efficient. In particular, the transient of the PSK:GO (0.05 mg mL^{-1}) sample has the smallest τ_1 value (2 ns) with a large relative amplitude (0.76), which explains that enhanced charge separation in the PSK:GO composite plays a key role in improving the device performance, as shown in Fig. 3. For the PSK:GO (0.075 mg mL^{-1}) sample, PL quenching was less efficient because the relative amplitude of τ_1 was much smaller than those of both other PSK:GO hybrid composite samples. This result indicates that GO at a large concentration in PSK would agglomerate (Fig. S7, ESI†) to impede the hole extraction, which deteriorates the device performance significantly. Moreover, we found that the slow decay feature in PSK was described with two decay components with time coefficients τ_2 and τ_3 in the PSK:GO samples, but the relative amplitudes were much smaller than that of τ_2 of the pristine PSK sample. The trend of relaxation times shows the order (0.05 mg mL^{-1}) < (0.025 mg mL^{-1}) < (0.075 mg mL^{-1}) for τ_2 but the reverse order (0.075 mg mL^{-1}) < (0.025 mg mL^{-1}) < (0.05 mg mL^{-1}) for τ_3. This result indicates that τ_2 is still related to hole extraction with the same trend as τ_1 but τ_3 might be related to the recombination in the bulk, for which the best PSK:GO hybrid composite cell (0.05 mg mL^{-1}) exhibits retarded recombination considering its great PV performance.

We recorded the electrochemical impedance spectra (EIS) to investigate the internal electrical processes under one-sun illumination and open-circuit conditions, which were introduced into the system of perovskite solar cells to monitor the interfacial changes.[51–55] The Nyquist plots of the pristine PSK and PSK:GO hybrid composite devices shown in Fig. 5 display typical semicircles in the frequency range of 100 mHz to 4 MHz. For all perovskite solar cells, two arcs are evident in the Nyquist plots, which can be well fitted with an equivalent circuit shown on top of Fig. 5; the corresponding fitted parameters are listed

in Table S7, ESI.† In general, three arcs might be produced in the Nyquist plots: the high-frequency (hf) arc might be associated with the charge transfer of selective contacts, the intermediate-frequency (if) arc might be related to the charge recombination in the photoactive layer and the low-frequency (lf) arc might be due to dielectric relaxation.[56–58] Such a feature appearing in the lf range with slow dynamics could be assigned to the dielectric relaxation process; it is a procedure governed by an interfacial ion reorganization or aligning dipoles under an external electrical field and further induces a charge
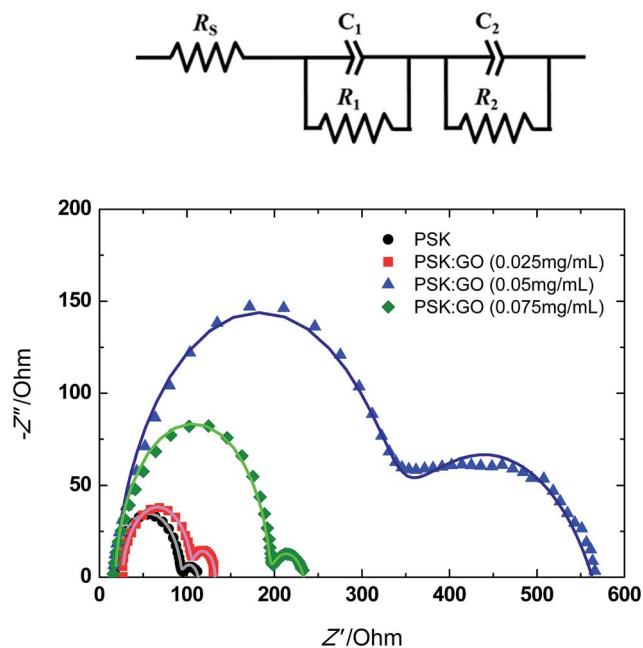

Fig. 5 Nyquist plots obtained from the electrochemical impedance spectra (EIS) of the pristine PSK and PSK:GO hybrid composite devices under one-sun illumination and open-circuit conditions. The scattered points are experimental data and the solid lines are curves fitted according to the equivalent circuit shown above.
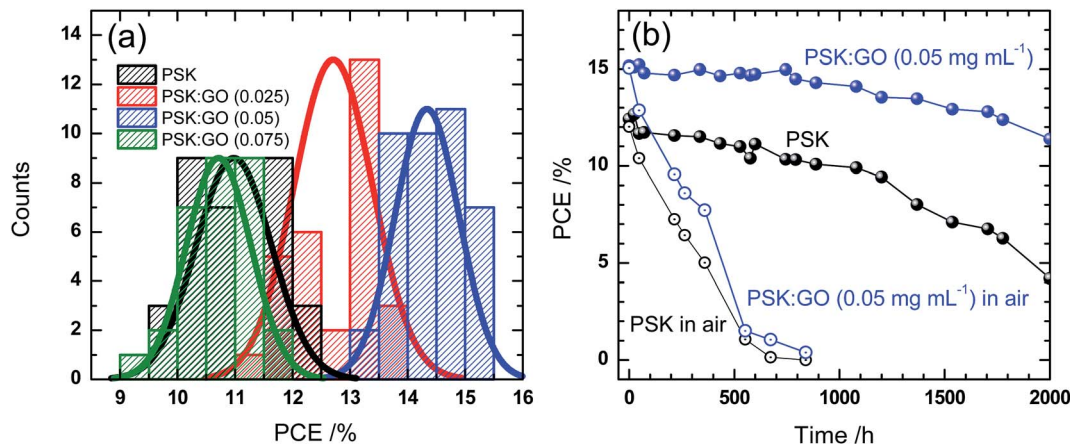
Fig. 6 (a) Histograms of the pristine PSK and PSK:GO hybrid composite inverted perovskite solar cells fabricated under the same experimental conditions. (b) Profiles of efficiency stability of the pristine PSK and PSK:GO hybrid composite devices as a function of storage period.

polarization which is intrinsic to the original properties of perovskites, *e.g.* different cations or halides. It is suggested that the dielectric relaxation is the charge rearrangement from a disordered distribution to an ordered distribution and creates a dipole which might be the main reason for charge accumulation (lower charge separation) in solar cells.[57,59] In our case, as only two arcs were observed in the Nyquist plots for all devices, which were not the hf arc, we attribute the two arcs to charge recombination and dielectric relaxation for which the corresponding impedances are R_1 and R_2, respectively.[50] Because the hole-selective contact (GO) and the electron-selective contact (PCBM) are the same for all pristine PSK and PSK:GO hybrid composite solar cells, the observed systematic variation of R_1 and R_2 values reflects the retarded charge recombination and decreased dielectric relaxation in the active layer in the order PSK:GO (0.05 mg mL^{-1}) > PSK:GO (0.075 mg mL^{-1}) > PSK:GO (0.025 mg mL^{-1}) > pristine PSK, consistent with the trend of the shunt resistance (R_{SH}) summarized in Table 1. All devices were fabricated with the same architecture, but R_2 systematically increased with increasing amount of GO inside the PSK nanocrystals until GO reached the optimal concentration (0.05 mg mL^{-1}). We attribute the increased R_2 in the 0.05 mg mL^{-1} device to the retardation of the dielectric relaxation and so the charge accumulation in that PSK:GO hybrid composite was minimized for improved charge separation.[50] Blending of GO into PSK thus had an effect both to decrease the rate of charge recombination (increasing V_{OC}) and to slow the dielectric relaxation (increasing J_{SC} and FF) in the PSK:GO active layer, producing the improved overall device performance observed in Fig. 3 except for the PSK:GO hybrid composite (0.075 mg mL^{-1}) device, for which the inhomogeneity of the hybrid film (Fig. S7, ESI†) led to a poor FF and worse performance than those of the other two hybrid composite devices.

Fig. 6a and b show histograms of the PCE and profiles of efficiency stability, respectively, to compare the reproducibility and stability of both pristine PSK and PSK:GO hybrid composite devices. The corresponding devices were fabricated under the same experimental conditions for solar cells of each type; the

photovoltaic parameters are listed in Tables S8–S11, ESI.† The average PCEs are 11.0 ± 0.7%, 12.7 ± 0.7%, 14.3 ± 0.6% and 10.7 ± 0.6% for pristine PSK, PSK:GO (0.025 mg mL^{-1}), PSK:GO (0.05 mg mL^{-1}) and PSK:GO (0.075 mg mL^{-1}), respectively. To test the long-term stability of the devices, we stored both pristine PSK and PSK:GO (0.05 mg mL^{-1}) solar cells in air (relative humidity 50%) and in a glovebox without encapsulation for a period of 2000 h. Fig. 6b shows that both devices suffered from rapid degradation of performance on storage in air, which originates from the sensitivity of the perovskite crystals to moisture under a relative humidity of 50%. In contrast, the performance of the PSK:GO hybrid composite solar cells in an inert atmosphere retained nearly 80% of the initial device value on storage over 2000 h whereas the pristine PSK device retained only half of its initial performance. The PV performance of the PSK:GO hybrid composite device in the glovebox was stable for the initial 800 h, showing an excellent intrinsic stability for solar cells of this type.

Conclusion

Graphene oxide (GO) served as a hole acceptor and the p-contact electrode in our constructed inverted hybrid composite perovskite solar cells with device architecture ITO/GO/PSK:GO/PCBM/Ag for PSK:GO composites with three GO concentrations, 0.025, 0.05 and 0.075 mg mL^{-1}. The presence of GO in the hybrid PSK:GO composite enhanced the charge separation, retarded the charge recombination and balanced the charge mobility to attain the best device performance with a PCE of 15.2% at a GO concentration 0.05 mg mL^{-1}, which is much greater than that of a GO-based planar heterojunction device (PCE 12.3%) without GO in the active layer. We emphasize the significant contribution of graphene oxide inside the PSK:GO composite layer in improving the photovoltaic performance with great reproducibility and stability *via* low-temperature and cost-effective solution-based fabrication, which offers prospective applications for flexible photovoltaic devices.

13962 | *J. Mater. Chem. A*, 2017, 5, 13957–13965

This journal is © The Royal Society of Chemistry 2017

Experimental section

Synthesis of graphene oxide

Graphene oxide was prepared by oxidation of natural graphite powder according to a modified Hummers' method.[41] Briefly, graphite powder (1.0 g) was sonicated in concentrated sulfuric acid (30 mL, 96–98%) at 23 °C for 1 h. $NaNO_3$ (0.5 g) was added under stirring ; the mixture was cooled in an ice bath. Under vigorous stirring, $KMnO_4$ (6.0 g) was added slowly. The reaction system was transferred to an oil bath (37–40 °C) for about 1 h. H_2O (200 mL) was added slowly, with stirring for another 30 min while the temperature was increased to 70–80 °C. In the final step, H_2O (200 mL) was added, followed by a slow addition of H_2O_2 (5–7 mL, 30%); in this stage, the colour of the solution changed from brown to yellow. The mixture was centrifuged and washed with HCl aqueous solution (5%), followed by repeated washing with H_2O and then with DMF. The resulting solid was dispersed in DMF with agitation followed by ultra-sonication. The obtained brown dispersion was centrifuged (30 min, 3000 rpm) to remove unreacted graphite or agglomerated sheets.

Preparation of the perovskite film

The synthesized CH_3NH_3I powder[60] was mixed with PbI_2 (Alfa Aesar) in a 1 : 1 molar ratio in anhydrous DMF at 70 °C for 3 h with a $CH_3NH_3PbI_3$ (PSK) concentration of 45 mass%. Graphene oxide was dispersed in DMF (concentration 0.5 mg mL^{-1}). A blended solution was prepared on mixing the stock solution of perovskite and graphene oxide solution. The concentration of perovskite in both pristine PSK solution and PSK:GO solution was fixed to 45 mass%; PSK:GO solutions were prepared with graphene oxide (GO) at mass concentrations of 0.025, 0.05 and 0.075 mg mL^{-1}. After the pre-cleaned ITO substrates were treated with UV–ozone for 18 min the GO layer was spin-coated on the ITO substrates at 4000 rpm (torsion rate: 12 000 rpm s^{-1}) with the GO solution of 0.5 mg mL^{-1} concentration, followed by annealing at 125 °C for 10 min. The perovskite films were deposited using the solvent-induced method.[6] Pristine PSK solution or PSK:GO solution was first spin-coated on top of the ITO/GO substrate at 5000 rpm (torsion rate: 10 000 rpm s^{-1}). With a delay period of 5 s, chlorobenzene was dropped on the substrate to promote rapid nucleation, followed by annealing at 100 °C for 2 min. The films were subjected to solvent annealing:[42] the perovskite film was kept under DMF vapor at 100 °C for 10 min. PCBM solution in chlorobenzene (2 mass%) was spin-coated on a pristine PSK layer or a PSK:GO hybrid composite layer at 1000 rpm (torsion rate: 1000 rpm s^{-1}) for 30 s to serve as an electron-transport layer. Ag (100 nm) was deposited by thermal evaporation in a vacuum system (pressure 5×10^{-6} Torr); with a metal mask the active area of the device was 0.0225 cm^2.

Characterization of materials and devices

A field-emission scanning electron microscope (FESEM, Hitachi SU8010) and atomic force microscope (VT SPM, SII Nanotechnology Inc.) were used to investigate the morphology and structure of the samples. The X-ray diffraction (XRD) patterns of the thin films coated on the ITO substrates were obtained with an X-ray diffractometer (Bruker AXS, D8 Advance, Cu Kα irradiation, $\lambda = 154.18$ pm). The Raman spectra of graphene oxide confirmed two lines at G (1605 cm^{-1}) and D (1339 cm^{-1}). The functional groups of various types were deduced from the infrared (FTIR) spectra of GO. The current density–voltage characteristics of the devices were recorded with a digital source meter (Keithley 2400) under one-sun illumination (AM 1.5G, 100 mW cm^{-2}) with a solar simulator (XES-40S1, SAN-E1), calibrated with a silicon diode and a KG-5 filter to decrease the mismatch of the spectrum. The spectra of incident photons to current (IPCE) were recorded with a system comprising a Xe lamp (A-1010, PTi, 150 W) and a monochromator (PTi). The absorption spectra of the thin-film and solution samples were recorded with a spectrophotometer (JASCO V-570).

The photoluminescence (PL) spectra were recorded in the range of 650–900 nm with excitation at 635 nm (LDH-635, PicoQuant). The PL transients were recorded with a time-correlated single-photon counting (TCSPC) system (Fluotime 200, PicoQuant, excitation at 635 nm) from a picosecond pulsed-diode laser (LDH-635, PicoQuant, FWHM ~ 70 ps). The repetition rate of the laser used for all experiments was 0.5 MHz and the pulse energy was 1 nJ cm^{-2}; the beam size was expanded to 1.5 mm × 3.5 mm. The PL temporal profiles were collected at 770 nm, which is the maximum for all the perovskite samples under investigation. The electrochemical impedance spectra (EIS) of all the devices were measured with an electrochemical workstation (IM 6, Zahner, Germany) over the frequency range of 100 mHz to 4 MHz with an ac amplitude of 10 mV under one-sun illumination and open-circuit conditions. The obtained EIS data were fitted (Z-view software) based on the equivalent circuit model. The mobilities and concentrations of the charge carriers of the perovskite films were measured with Hall effect equipment (Nanometrics HL5500 Hall system) performed with four-square gold contacts at the corners. The perovskite films were measured under a magnetic field of 0.5 T and a constant DC current.

References

1 A. Kojima, K. Teshima, Y. Shirai and T. Miyasaka, *J. Am. Chem. Soc.*, 2009, **131**, 6050–6051.

2 M. M. Lee, J. Teuscher, T. Miyasaka, T. N. Murakami and H. J. Snaith, *Science*, 2012, **338**, 643–647.

3 H. S. Kim, C. R. Lee, J. H. Im, K. B. Lee, T. Moehl, A. Marchioro, S. J. Moon, R. Humphry-Baker, J. H. Yum, J. E. Moser, M. Grätzel and N. G. Park, *Sci. Rep.*, 2012, **2**, 591–597.

4 J. H. Heo, S. H. Im, J. H. Noh, T. N. Mandal, C. S. Lim, J. A. Chang, Y. H. Lee, H. j. Kim, A. Sarkar,

This journal is © The Royal Society of Chemistry 2017

J. Mater. Chem. A, 2017, **5**, 13957–13965 | **13963**

M. K. Nazeeruddin, M. Gratzel and S. I. Seok, *Nat. Photonics*, 2013, **7**, 486–491.

5 H. Zhou, Q. Chen, G. Li, S. Luo, T. b. Song, H. S. Duan, Z. Hong, J. You, Y. Liu and Y. Yang, *Science*, 2014, **345**, 542–546.

6 M. Xiao, F. Huang, W. Huang, Y. Dkhissi, Y. Zhu, J. Etheridge, A. Gray-Weale, U. Bach, Y. B. Cheng and L. Spiccia, *Angew. Chem., Int. Ed.*, 2014, **126**, 10056–10061.

7 N. J. Jeon, J. H. Noh, Y. C. Kim, W. S. Yang, S. Ryu and S. I. Seok, *Nat. Mater.*, 2014, **13**, 897–903.

8 J. Burschka, N. Pellet, S. J. Moon, R. Humphry-Baker, P. Gao, M. K. Nazeeruddin and M. Gratzel, *Nature*, 2013, **499**, 316–319.

9 Z. Xiao, C. Bi, Y. Shao, Q. Dong, Q. Wang, Y. Yuan, C. Wang, Y. Gao and J. Huang, *Energy Environ. Sci.*, 2014, **7**, 2619–2623.

10 W. S. Yang, J. H. Noh, N. J. Jeon, Y. C. Kim, S. Ryu, J. Seo and S. I. Seok, *Science*, 2015, **348**, 1234–1237.

11 N. Ahn, D. Y. Son, I. H. Jang, S. M. Kang, M. Choi and N. G. Park, *J. Am. Chem. Soc.*, 2015, **137**, 8696–8699.

12 J. H. Heo, H. J. Han, D. Kim, T. K. Ahn and S. H. Im, *Energy Environ. Sci.*, 2015, **8**, 1602–1608.

13 M. Saliba, T. Matsui, K. Domanski, J. Y. Seo, A. Ummadisingu, S. M. Zakeeruddin, J.-P. Correa-Baena, W. R. Tress, A. Abate, A. Hagfeldt and M. Grätzel, *Science*, 2016, **354**, 206–209.

14 National Renewable Energy Laboratory (NREL), http://www.nrel.gov/ncpv/, 2017.

15 E. L. Unger, E. T. Hoke, C. D. Bailie, W. H. Nguyen, A. R. Bowring, T. Heumuller, M. G. Christoforo and M. D. McGehee, *Energy Environ. Sci.*, 2014, **7**, 3690–3698.

16 H. J. Snaith, A. Abate, J. M. Ball, G. E. Eperon, T. Leijtens, N. K. Noel, S. D. Stranks, J. T. W. Wang, K. Wojciechowski and W. Zhang, *J. Phys. Chem. Lett.*, 2014, **5**, 1511–1515.

17 H. S. Kim and N. G. Park, *J. Phys. Chem. Lett.*, 2014, **5**, 2927–2934.

18 N. G. Park, M. Grätzel, T. Miyasaka, K. Zhu and K. Emery, *Nat. Energy*, 2016, **1**, 16152.

19 T. Leijtens, B. Lauber, G. E. Eperon, S. D. Stranks and H. J. Snaith, *J. Phys. Chem. Lett.*, 2014, **5**, 1096–1102.

20 C. Roldan-Carmona, O. Malinkiewicz, A. Soriano, G. MinguezEspallargas, A. Garcia, P. Reinecke, T. Kroyer, M. I. Dar, M. K. Nazeeruddin and H. J. Bolink, *Energy Environ. Sci.*, 2014, **7**, 994–997.

21 E. Edri, S. Kirmayer, A. Henning, S. Mukhopadhyay, K. Gartsman, Y. Rosenwaks, G. Hodes and D. Cahen, *Nano Lett.*, 2014, **14**, 1000–1004.

22 E. Edri, S. Kirmayer, S. Mukhopadhyay, K. Gartsman, G. Hodes and D. Cahen, *Nat. Commun.*, 2014, **5**, 3461–3468.

23 N. S. Sariciftci, L. Smilowitz, A. J. Heeger and F. Wudl, *Science*, 1992, **258**, 1474–1476.

24 G. Yu, J. Gao, J. C. Hummelen, F. Wudl and A. J. Heeger, *Science*, 1995, **270**, 1789–1791.

25 A. J. Heeger, *Angew. Chem., Int. Ed.*, 2001, **40**, 2591–2611.

26 C.-H. Chiang and C.-G. Wu, *Nat. Photonics*, 2016, **10**, 196–200.

27 K. Wang, C. Liu, P. Du, J. Zheng and X. Gong, *Energy Environ. Sci.*, 2015, **8**, 1245–1255.

28 C. Liu, K. Wang, P. Du, C. Yi, T. Meng and X. Gong, *Adv. Energy Mater.*, 2015, **5**, 1402024.

29 J. Xu, A. Buin, A. H. Ip, W. Li, O. Voznyy, R. Comin, M. Yuan, S. Jeon, Z. Ning, J. J. McDowell, P. Kanjanaboos, J. P. Sun, X. Lan, L. N. Quan, D. H. Kim, I. G. Hill, P. Maksymovych and E. H. Sargent, *Nat. Commun.*, 2015, **6**, 7081.

30 H. Ma, H. L. Yip, F. Huang and A. K. Y. Jen, *Adv. Funct. Mater.*, 2010, **20**, 1371–1388.

31 L. M. Chen, Z. Hong, G. Li and Y. Yang, *Adv. Mater.*, 2009, **21**, 1434–1449.

32 J. You, Z. Hong, Y. Yang, Q. Chen, M. Cai, T. B. Song, C. C. Chen, S. Lu, Y. Liu, H. Zhou and Y. Yang, *ACS Nano*, 2014, **8**, 1674–1680.

33 P. W. Liang, C. Y. Liao, C. C. Chueh, F. Zuo, S. T. Williams, X. K. Xin, J. Lin and A. K. Y. Jen, *Adv. Mater.*, 2014, **26**, 3748–3754.

34 J. M. Yun, J. S. Yeo, J. Kim, H. G. Jeong, D. Y. Kim, Y. J. Noh, S. S. Kim, B. C. Ku and S. I. Na, *Adv. Mater.*, 2011, **23**, 4923–4928.

35 M. Jørgensen, K. Norrman and F. C. Krebs, *Sol. Energy Mater. Sol. Cells*, 2008, **92**, 686–714.

36 F. Bonaccorso, Z. Sun, T. Hasan and A. C. Ferrari, *Nat. Photonics*, 2010, **4**, 611–622.

37 J. S. Yeo, J. M. Yun, Y. S. Jung, D. Y. Kim, Y. J. Noh, S. S. Kim and S. I. Na, *J. Mater. Chem. A*, 2014, **2**, 292–298.

38 J. S. Yeo, R. Kang, S. Lee, Y. J. Jeon, N. Myoung, C. L. Lee, D. Y. Kim, J. M. Yun, Y. H. Seo, S. S. Kim and S. I. Na, *Nano Energy*, 2015, **12**, 96–104.

39 Z. Wu, S. Bai, J. Xiang, Z. Yuan, Y. Yang, W. Cui, X. Gao, Z. Liu, Y. Jin and B. Sun, *Nanoscale*, 2014, **6**, 10505–10510.

40 J. K. Kim, S. J. Kim, M. J. Park, S. Bae, S.-P. Cho, Q. G. Du, D. H. Wang, J. H. Park and B. H. Hong, *Sci. Rep.*, 2015, **5**, 14276–14285.

41 W. S. Hummers and R. E. Offeman, *J. Am. Chem. Soc.*, 1958, **80**, 1339.

42 Z. Xiao, Q. Dong, C. Bi, Y. Shao, Y. Yuan and J. Huang, *Adv. Mater.*, 2014, **26**, 6503–6509.

43 Y. Zhang, X. D. Dang, C. Kim and T. Q. Nguyen, *Adv. Energy Mater.*, 2011, **1**, 610–617.

44 C. Bi, Y. Shao, Y. Yuan, Z. Xiao, C. Wang, Y. Gao and J. Huang, *J. Mater. Chem. A*, 2014, **2**, 18508–18514.

45 C. C. Stoumpos, C. D. Malliakas and M. G. Kanatzidis, *Inorg. Chem.*, 2013, **52**, 9019–9038.

46 C. Wehrenfennig, M. Liu, H. J. Snaith, M. B. Johnston and L. M. Herz, *Energy Environ. Sci.*, 2014, **7**, 2269–2275.

47 Q. Dong, Y. Fang, Y. Shao, P. Mulligan, J. Qiu, L. Cao and J. Huang, *Science*, 2015, **347**, 967–970.

48 C. S. Ponseca, T. J. Savenije, M. Abdellah, K. Zheng, A. Yartsev, T. Pascher, T. Harlang, P. Chabera, T. Pullerits, A. Stepanov, J.-P. Wolf and V. Sundström, *J. Am. Chem. Soc.*, 2014, **136**, 5189–5192.

49 D. Shi, V. Adinolfi, R. Comin, M. Yuan, E. Alarousu, A. Buin, Y. Chen, S. Hoogland, A. Rothenberger, K. Katsiev, Y. Losovyj, X. Zhang, P. A. Dowben, O. F. Mohammed, E. H. Sargent and O. M. Bakr, *Science*, 2015, **347**, 519–522.

50 B. Wang, K. Y. Wong, S. Yang and T. Chen, *J. Mater. Chem. A*, 2016, **4**, 3806–3812.

51 B. Suarez, V. Gonzalez-Pedro, T. S. Ripolles, R. S. Sanchez, L. Otero and I. Mora-Sero, *J. Phys. Chem. Lett.*, 2014, **5**, 1628–1635.

52 V. Gonzalez-Pedro, E. J. Juarez-Perez, W.-S. Arsyad, E. M. Barea, F. Fabregat-Santiago, I. Mora-Sero and J. Bisquert, *Nano Lett.*, 2014, **14**, 888–893.

53 H. S. Kim, I. Mora-Sero, V. Gonzalez-Pedro, F. Fabregat-Santiago, E. J. Juarez-Perez, N. G. Park and J. Bisquert, *Nat. Commun.*, 2013, **4**, 2242–2248.

54 J. A. Christians, R. C. M. Fung and P. V. Kamat, *J. Am. Chem. Soc.*, 2014, **136**, 758–764.

55 A. Dualeh, T. Moehl, N. Tétreault, J. Teuscher, P. Gao, M. K. Nazeeruddin and M. Grätzel, *ACS Nano*, 2014, **8**, 362–373.

56 J. Bisquert, L. Bertoluzzi, I. Mora-Sero and G. Garcia-Belmonte, *J. Phys. Chem. C*, 2014, **118**, 18983–18991.

57 R. S. Sanchez, V. Gonzalez-Pedro, J.-W. Lee, N.-G. Park, Y. S. Kang, I. Mora-Sero and J. Bisquert, *J. Phys. Chem. Lett.*, 2014, **5**, 2357–2363.

58 G. Garcia-Belmonte, A. Munar, E. M. Barea, J. Bisquert, I. Ugarte and R. Pacios, *Org. Electron.*, 2008, **9**, 847–851.

59 L. Zheng, Y. Ma, L. Xiao, F. Zhang, Y. Wang and H. Yang, *ACS Appl. Mater. Interfaces*, 2017, **9**, 14129–14135.

60 K.-C. Wang, J.-Y. Jeng, P.-S. Shen, Y.-C. Chang, E. W.-G. Diau, C.-H. Tsai, T.-Y. Chao, H.-C. Hsu, P.-Y. Lin, P. Chen, T.-F. Guo and T.-C. Wen, *Sci. Rep.*, 2014, **4**, 4756–4763.